Article

Rational Design of a Cost-Effective Biomass Carbon Framework for High-Performance Lithium Sulfur Batteries

Zhongchao Bai [1], Kai Fan [2], Meiqing Guo [3], Mingyue Wang [4,*], Ting Yang [5] and Nana Wang [4,*]

1. Institute of Energy Materials Science, University of Shanghai for Science and Technology, Shanghai 200093, China; baizhongchao@tyut.edu.cn
2. College of Mechanical and Electronic Engineering, Shandong University of Science and Technology, Qingdao 266590, China; 202083050115@sdust.edu.cn
3. Institute of Applied Mechanics, College of Mechanical and Vehicle Engineering, Taiyuan University of Technology, Taiyuan 030024, China; guomeiqing@tyut.edu.cn
4. Institute for Superconducting and Electronic Materials, Australian Institute for Innovative Materials, Innovation Campus, University of Wollongong, Squires Way, North Wollongong, NSW 2500, Australia
5. Department of Applied Chemistry, Yuncheng University, Yuncheng 044000, China; yangting@ycu.edu.cn
* Correspondence: mw663@uowmail.edu.au (M.W.); nanaw@uow.edu.au (N.W.)

Abstract: Lithium–sulfur (Li-S) batteries are the most attractive candidates for next-generation large-scale energy storage because of their high theoretical energy density and the affordability of sulfur. However, most of the reported research primarily concentrates on low sulfur loading (below 2 mg_s cm^{-2}) cathodes using binders and traditional collectors, thus undermining the expected energy density. Herein, a N, O co-doped carbon nanotube (N, O-CNT) decorated wood framework (WF), denoted as WF-CNT, was designed as a free-standing sulfur host, achieving high sulfur loading of 10 mg_s cm^{-2}. This unique cathode featured low tortuosity microchannels and a conductive framework, reducing the diffusion paths for both ions and electrons and accommodating the volume changes associated with sulfur. Moreover, the internal CNT forests effectively captured soluble lithium polysulfides (LiPSs) and catalyze their redox kinetic. Consequently, the S@WF-CNT-800 sample exhibited a high initial discharge capacity of 1438.2 mAh g^{-1} at a high current density of 0.5 A g^{-1}. Furthermore, a reversible capacity of 404.5 mAh g^{-1} was obtained after 500 cycles with sulfur loading of 5 mg_s cm^{-2} at 0.5 A g^{-1}. This work may support the development of high sulfur loading cathodes utilizing cost-effective and sustainable biomass materials for Li-S batteries.

Keywords: lithium sulfur batteries; wood framework; high sulfur loading; low-tortuosity microchannel

1. Introduction

With the rapid and remarkable development of the electric vehicle and portable electronics markets in recent years, there has been an extraordinary surge in the demand for high-energy-density solutions, prompting intensive exploration into advanced alternatives that can potentially supersede conventional lithium-ion batteries (LIBs) [1–3]. Among these innovative alternatives, lithium–sulfur (Li-S) batteries have emerged as exceptionally promising candidates for the next generation of rechargeable battery technology. The attraction of Li-S batteries lies in their outstanding theoretical capacity, which stands at an impressive 1675 mAh g^{-1}, and their remarkably high theoretical energy density, which reaches a remarkable 2567 Wh kg^{-1} [4–7]. Moreover, sulfur, a key component of Li-S batteries, holds distinct advantages in terms of cost-effectiveness, environmental safety, and its abundant availability in nature [8–10]. Hence, there is a growing interest in and focus on Li-S batteries. Nevertheless, despite their immense promise, the practical implementation of Li-S batteries remains encumbered by several formidable challenges that are yet to be entirely surmounted. These challenges primarily stem from the inherent insulating nature of sulfur and its discharge products, impeding the efficient utilization

of the active material. Additionally, the large volume change experienced during the charge–discharge cycles exerts mechanical stress on the battery components, which can lead to structural degradation and reduced overall performance. Another substantial obstacle is the shuttle effect, which intensifies the depletion of the active material, accelerates capacity deterioration, and restricts the cycling lifespan of Li-S batteries [11–13]. These formidable drawbacks underscore the need for continued research and innovation to unlock the full potential of Li-S batteries and address these critical challenges.

To tackle these issues, numerous approaches have been explored and implemented. These efforts encompass a broad spectrum of strategies, including the innovative design and fine-tuning of sulfur cathodes [14–18], the integration of specially engineered separators with protective coatings [19–22], the introduction of novel additives into the electrolyte composition [23–25], the design of polymer/solid-state electrolytes [26,27], and the development of rational techniques to safeguard lithium metal anodes [28–30]. One particularly promising avenue has been the confinement of sulfur species within conductive carbon hosts, a widely studied approach that has proven to be effective in curbing the relentless shuttle of lithium polysulfides (LiPSs) and enhancing the electrochemical utilization of active materials within the cathode structure. Despite the significant progress achieved through these endeavors, it is worth noting that much of the current research primarily centers around low sulfur loading levels, typically falling below 2 mg_s cm^{-2}, which falls far short of achieving the ultimate goal of high energy density [31,32]. Consequently, there arises a pressing need to redirect our focus towards high sulfur loading cathodes as these offer the potential to substantially increase energy capacity. In fact, the inherent challenges posed by Li-S batteries are amplified when it comes to handling high sulfur loading. During the cyclic operation of the battery, the diffusion of LiPSs becomes notably more pronounced, resulting in a reduction in the electrochemical utilization of the active materials and hastening the degradation of the cathode [33,34]. Moreover, the traditional collectors and binders used in these systems add considerable weight, partially offsetting the expected energy density enhancements associated with high sulfur loading. Therefore, the development of a practical and free-standing sulfur cathode emerges as a pivotal imperative in the quest to optimize the performance of Li-S batteries with high sulfur loading.

Recently, various sustainable precursors have been explored for their cost-effectiveness in electrode production [35–37]. Wood, acknowledged as a renewable biomass resource, emerges as an appealing choice for the creation of robust, self-supporting carbon electrodes. This preference is rooted in its inherent qualities, including a naturally layered and porous structure, exceptional mechanical strength, and minimal bending curvature [38,39]. These distinctive qualities position wood as an ideal starting material for the development of advanced electrode systems. One illustrative example of the potential of wood-derived materials is found in the work of Hu et al. They successfully engineered a low-tortuosity carbon framework (CF) characterized by high conductivity and low weight by directly carbonizing natural wood. This CF served as an ultrathick electrode host, leading to the realization of high-capacity LIBs with remarkable performance characteristics [40]. In this work, poplar wood was thoughtfully chosen as the precursor material for the creation of a wood framework (WF) host. To augment the affinity between carbon and LiPSs, this WF underwent a process of embellishment with nitrogen and oxygen co-doped carbon nanotubes (N, O-CNT). This enhancement resulted in the formation of a CNT forest grown at the tips of the WF (WF-CNT). Remarkably, thanks to its outstanding conductivity and enduring wood-like structural integrity, this composite material can function as an accommodating host for high sulfur loading, labeled as S@WF-CNT. Notably, this design eliminates the necessity for conventional components such as a current collector, conductive additives, or binders in the cathode assembly via a facile method. The distinctive S@WF-CNT cathodes are characterized by their low-tortuosity microchannels, a feature that significantly reduces the diffusion pathways for both ions and electrons. This architectural choice not only facilitates the unrestricted movement of the electrolyte within the cathode but also adeptly manages the volumetric changes associated with the sulfur component.

Furthermore, the internal N, O co-doped CNT forests play a pivotal role in effectively capturing soluble LiPSs and catalyzing their redox reactions within the electrode, attributed to the nonpolar–polar interaction. As a result, the S@WF-CNT-800 sample exhibits an initial discharge capacity of 1438.2 mAh g^{-1} and delivers a high capacity of 588.6 mAh g^{-1} after 100 cycles at a high current density of 0.5 A g^{-1}. Furthermore, S@WF-CNT-800 electrodes with impressive areal sulfur loading of 5 and 10 mg$_s$ cm^{-2} can be achieved. A reversible capacity of 404.5 mAh g^{-1} is obtained after 500 cycles with a sulfur loading of 5 mg$_s$ cm^{-2} at 0.5 A g^{-1}. This approach provides valuable insights for advancing the development of high-energy-density Li-S batteries through a straightforward method utilizing biomass precursors.

2. Experimental Section

2.1. Preparation of WF-CNT

All acquired materials were utilized in their original state without additional purification. Cobalt (II) acetate tetrahydrate, sulfur powder, 1-Methyl-2-pyrrolidinone (NMP), and melamine were bought from MACKLIN (Shanghai, China). First, cobalt acetate (1.2 g) was dissolved in deionized water (5 mL) with agitation at room temperature for 6 h under magnetic stirring to form a homogeneous solution, which appeared deep red in color. Next, poplar wood slices with a diameter of 0.5 cm were cut using a microtome followed by drying at 60 °C in the oven. Then, poplar wood slices were immersed in the above cobalt acetate solution. After soaking for 12 h, they were removed and dried for 6 h. Both the soaking and drying processes were repeated three times. Next, the treated poplar wood was positioned downstream of 1.2 g of melamine powder within a tube furnace, with melamine acting as both the carbon and nitrogen source for the growth of CNTs on the WF. The temperature was first raised to 180 °C for 2 h and then further increased at a rate of 2 °C min^{-1} to reach 600, 700, 800, and 900 °C for 4 h to yield the final product. Notably, CNT could not grow when the pyrolysis temperature was 600 °C, which is denoted as WF-600. The other three samples are denoted as WF-CNT-700, WF-CNT-800, and WF-CNT-900, respectively.

2.2. Preparation of S@WF-CNT

Initially, the equivalent mass of sulfur was subjected to a melting process at 160 °C on a hotplate. Subsequently, the molten sulfur was effortlessly absorbed into the WF-CNT framework (WF-600, WF-CNT-700, WF-CNT-800, and WF-CNT-900) due to its exceptional sulfur-affinitive properties. All these procedures were carried out within a glovebox. Following this, the composite was transferred into a vial and subjected to a temperature of 155 °C for a duration of 12 h, facilitating further impregnation and yielding the ultimate product S@WF-CNT (S@WF-600, S@WF-CNT-700, S@WF-CNT-800, and S@WF-CNT-900).

2.3. Characterization

The sample morphology was analyzed using scanning electron microscopy (SEM, Hitachi SU7000, Kyoto, Japan). The crystal structure was analyzed through X-ray diffraction (XRD, Thermo Ultima IV, Waltham, MA, USA) using a Cu K-alpha $\lambda = 0.154056$ nm monochromator. The scanning occurred in the 2θ angle range of 10–80° at a scan speed of 6°/min. Thermogravimetric analysis (TGA) was conducted to measure sulfur content with a Shimadzu (Kyoto, Japan) DTG-60H thermogravimetric analyzer. The temperature range extended from room temperature to 400 °C with a heating rate of 10 °C/min under a nitrogen atmosphere. X-ray photoelectron spectroscopy (XPS, Thermo ESCALAB 250XI, Waltham, MA, USA) was employed to characterize the surface chemical properties. Brunauer–Emmett–Teller (BET, Micromeritics ASAP2460, Shanghai, China) analysis was utilized to determine the specific surface area.

2.4. Electrochemical Measurement

CR2032 coin cells were assembled within an argon-filled glovebox for the Li-S electrochemical performance testing. Lithium metal was utilized as the anode, Celgard

2320 (SINERO, Suzhou, China) served as the separator, and a 1 M solution of lithium bis(trifluoromethane)sulfonimide (LiTFSI) in a solvent blend of dioxolane and dimethoxyethane (DOL/DME, volume ratio 1:1) supplemented with 1 wt% $LiNO_3$ was employed as the electrolyte. For the cathode sulfur loading at 2 mg cm^{-2}, the electrolyte-to-sulfur (E/S) ratio was 20 $\mu L/mg_s$. For sulfur loadings at 5 and 10 mg cm^{-2}, the corresponding electrolyte amounts were 100 and 200 μL, respectively. The half cells were activated through three cycles at 0.01–1 V, with a current density of 0.05 mA cm^{-2} for three cycles before conducting the test. Cycling and the rate performance were evaluated using a BST-5V20mA battery tester at room temperature. Five identical cells were made for each case of electrochemical measurement. Cyclic voltammetry (CV) and electrochemical impedance spectroscopy (EIS) measurements were carried out on an electrochemical workstation (CHI660E). The scanning rate for the CV test was 0.1 mV s^{-1} within the voltage range of 1.8–2.8 V. Additionally, the frequency for the EIS test ranged from 10 Hz to 100 kHz.

3. Results and Discussion

3.1. Morphology and Structure Characterization

The synthesis of the S@WF-CNT composite involved a well-defined and straightforward tip-growth CNT fabrication process, as illustrated in Figure 1. The starting point of this innovative approach was the selection of poplar wood as the primary precursor material. Poplar wood was chosen for its unique structural characteristics, widespread availability, and economical nature, making it an ideal candidate for this purpose. To introduce N, O co-doped CNTs to the WF, the poplar wood slices underwent a pivotal immersion step in a solution containing cobalt acetate. Cobalt ions in this solution played a critical role as catalysts for the subsequent CNT growth process. The resulting WF-CNT composite was formed through a controlled heat-treatment method conducted at various temperatures, including 600, 700, 800, and 900 °C. During this process, melamine was strategically employed to serve as both a carbon source and a nitrogen source. One of the key advantages of this composite lies in its creation of low-tortuosity microchannels, which serve to reduce the diffusion paths of ions or electrons, facilitate the unhindered transportation of electrolytes within the cathode, and accommodate the volumetric changes that occur during the cycle processes. Additionally, the CNT forest that forms within the structure provides multiple electron transfer pathways and a significantly increased specific surface area. These attributes are instrumental in achieving a high sulfur loading capacity within the composite while simultaneously mitigating the shuttle effect of LiPS, ultimately contributing to its exceptional electrochemical performance. Importantly, this synthesis method using a wood biomass precursor offers a more cost-effective and accessible approach, ultimately resulting in a thicker and more efficient electrode for energy storage applications.

In order to comprehensively explore the influence of varying heat temperatures on the material morphology, a systematic SEM analysis was carried out, which is illustrated in Figures 2a–c, S1 and S2. Throughout this examination, it became evident that the porous structure of the poplar wood remained remarkably unchanged across all samples, irrespective of the temperature conditions applied during the fabrication process. Interestingly, at temperatures up to 600 °C, no noticeable formation of CNTs was observed within the material structure. However, as the temperature rose above 700 °C, a significant transformation became apparent, characterized by the emergence of CNT growth on the surfaces of the parallel channels. By magnifying the marked area in Figure 2b, WF-CNT-800 stood out for its formation of more consistent and longer CNT forests (Figure 2c), which effectively enveloped the walls of the parallel channels. As shown in Figure S2, the WF-CNT-800 sample comprised uniform, parallel channels with a diameter ranging from 8 to 16 μm. This notable development holds great promise as it has the potential to create additional electron transfer pathways within the material and significantly amplify the specific surface area. These enhancements, in turn, could pave the way for increased sulfur loading within the composite material, ultimately contributing to the effective mitigation of the shuttle effect of

LiPSs during battery operation [41]. As the temperature was elevated to 800 and 900 °C, a notable change in the behavior of CNTs was observed, characterized by a reduction in CNT length. This alteration in CNT morphology resulted in less competitive electron transport compared to the WF-CNT-800 sample. Consequently, the WF-CNT-800 sample stood out as the most promising candidate in terms of electrochemical performance, a topic that will be further elaborated upon in the subsequent discussion. Moreover, complementary SEM energy dispersive spectroscopy (SEM-EDS) mapping images, as depicted in Figure 2d–i, provided compelling evidence of the even distribution of C, N, O, Co, and S throughout the WF-CNT-800 composite. This uniform distribution further underscored the success of the fabrication process in creating a well-balanced and comprehensive composite material, where the distinct elements were consistently distributed.
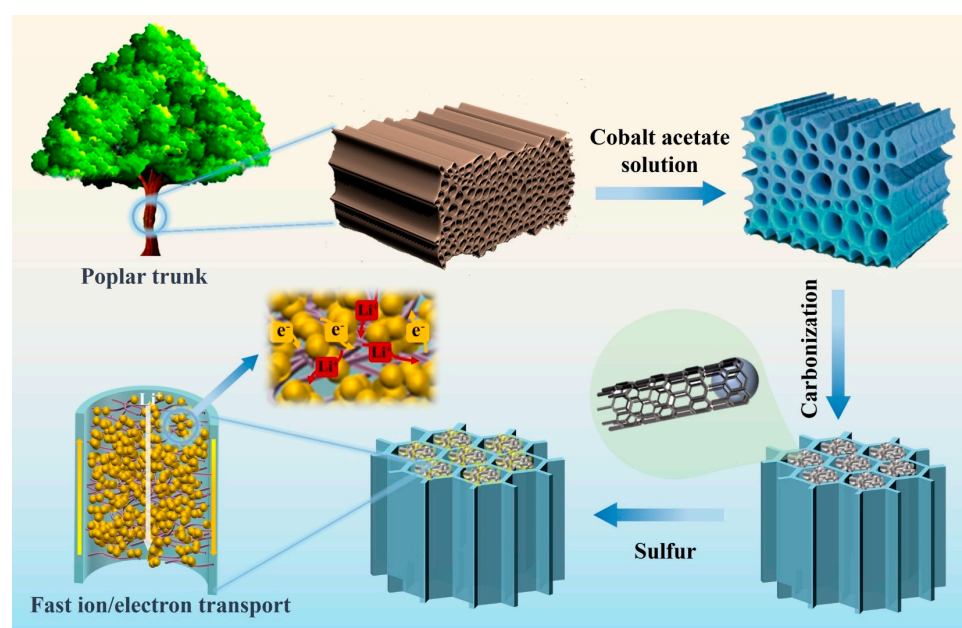

Figure 1. Schematic illustration of the synthesis process of S@WF-CNT electrodes.

The intricate porous characteristics of the WF-CNT samples were determined and analyzed through nitrogen adsorption–desorption isotherms, which is illustrated in Figure 3a. These isotherms unveiled a distinctive Type IV behavior accompanied by discernible hysteresis loops within the relative pressure range (P/P_0) spanning from 0.5 to 1.0. This characteristic behavior served as a strong indicator of a mesoporous structure, which is highly desirable for numerous applications [42]. Among the WF-CNT samples, WF-CNT-800 took the spotlight by offering the most extensive surface area, quantified at a remarkable 529.8 m^2 g^{-1}, as determined through the BET method. Notably, the pore size distribution, as depicted in Figure 3b, was centered around 2.73 nm, providing an abundance of active sites well-suited to the loading of sulfur. In contrast, the surface areas of WF-CNT-700 and WF-CNT-900 measured at 270.5 m^2 g^{-1} and 181.8 m^2 g^{-1}, respectively. This disparity in surface area underscored the pronounced advantages offered by the porous structure of the WF-CNT-800 sample, making it an ideal candidate for efficient sulfur infiltration. In Figure 3c, the XRD patterns of both the WF-CNT-800 and S@WF-CNT-800 composites are presented. Within the XRD pattern of WF-CNT-800, three distinct peaks at 2θ angles of 44.2°, 51.5°, and 75.9° corresponded to the (111), (200), and (220) lattice planes of cobalt (PDF#15-0806), respectively. Upon sulfur loading, the XRD pattern of the composite revealed the emergence of four characteristic peaks positioned at 2θ values approximately at 23.2°, 26.0°, 27.8°, and 28.8°. These peaks corresponded to the (222), (026), (206), and (135) lattice planes of sulfur (PDF#42-1278), clearly indicating the successful loading of sulfur into the composite structure. Figure 3d shows the TGA curve, providing vital insights into the sulfur loading within the composite material. The TGA

curve demonstrates that the mass of sulfur loaded into the composite amounted to 74.3%, a figure that surpasses the majority of research findings in this domain. This substantial sulfur loading is indicative of the exceptional potential of the WF-CNT-800 composite in accommodating a substantial quantity of sulfur, a highly desirable attribute for various applications, particularly in advanced energy storage systems.
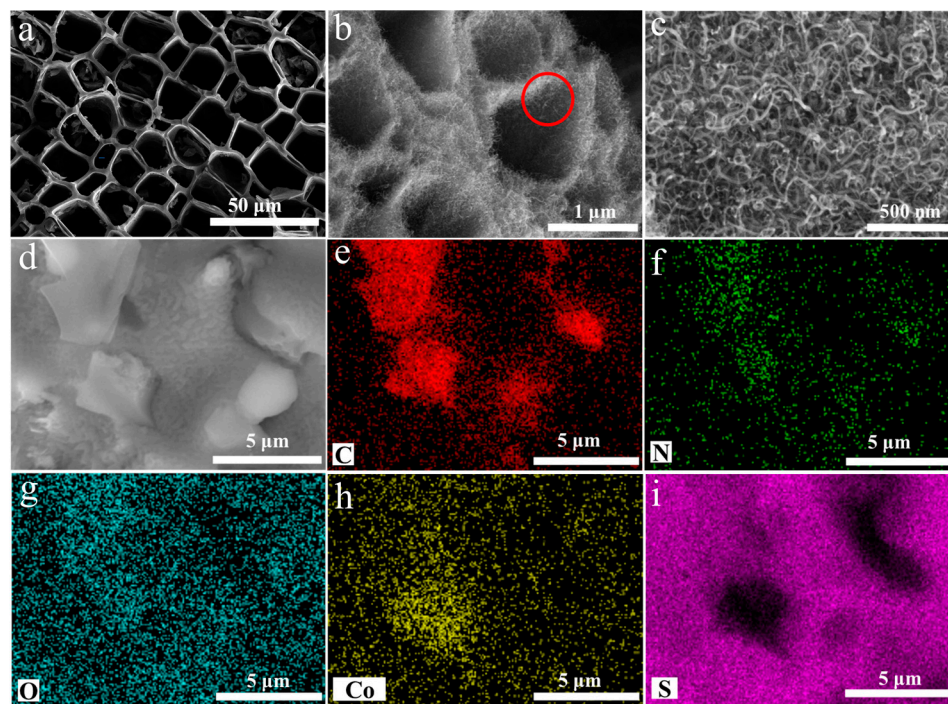

Figure 2. (**a–c**) SEM images of the WF-CNT-800 host and (**d–i**) SEM image with corresponding EDS maps of S@WF-CNT-800 cathode.

To delve deeper into the composition and surface chemical structure of the S@WF-CNT-800 sample, an in-depth analysis was conducted using XPS. The XPS survey spectrum, as depicted in Figure 4a, provided a comprehensive view of the elemental composition, clearly revealing the presence of C, N, O, Co, and S elements. Further scrutiny of the high-resolution XPS spectra offered invaluable insights into the chemical states and bonding configurations of these elements. The high-resolution XPS spectrum of Co $2p$, presented in Figure 4b, unveiled six major peaks, corresponding to the Co $2p_{3/2}$, Co $2p_{1/2}$, and satellite peaks. This spectrum could be further deconvoluted to discern different valence states. Notably, two distinct peaks at 797.4 and 781.5 eV could be attributed to the $2p_{1/2}$ and $2p_{3/2}$ states of Co^{2+}. Additionally, the presence of Co^{3+} states was also evident, as indicated by energy levels of 794.7 and 778.9 eV for $2p_{1/2}$ and $2p_{3/2}$, respectively [43]. This comprehensive understanding of the cobalt states is pivotal in elucidating the role of cobalt in the composite material. The high-resolution C $1s$ spectrum, presented in Figure 4c, exhibited three distinct peaks at 284.7, 285.5, and 289 eV. These peaks could be attributed to specific bonding configurations, such as C–C, C–N, and C=O bonds, offering insights into the carbon chemistry within the composite. Moving on to the high-resolution O $1s$ spectrum, as shown in Figure 4d, three discernible peaks at 533.5, 532, and 530.1 eV came into view. These peaks were associated with C–OH/C–O–C, C=O, and quinone/pyridone bonds, respectively, shedding light on the various oxygen-containing functional groups present in the composite. The high-resolution N $1s$ spectrum, displayed in Figure 4e, could be deconvoluted into three peaks situated at 401.2, 400.4, and 398.7 eV, corresponding to graphitic N, pyrrolic N, and pyridinic N [44]. Lastly, the high-resolution S $2p$ spectrum, as shown in Figure 4f, highlighted two strong splitting peaks centered at 163.9 and 165.2 eV. These peaks represented the S $2p_{3/2}$ and S $2p_{1/2}$ states of elemental sulfur [45]. This

observation reaffirmed the presence of elemental sulfur in the composite. According to the findings derived from the XPS analysis, the composite exhibited specific concentrations of doped nitrogen and oxygen atoms, quantified at 1.8 and 10.8 atomic percent (at. %), respectively. This deliberate doping enhanced the chemical interaction of the composite with LiPSs, ultimately playing a pivotal role in improving the overall performance of Li–S batteries [46].
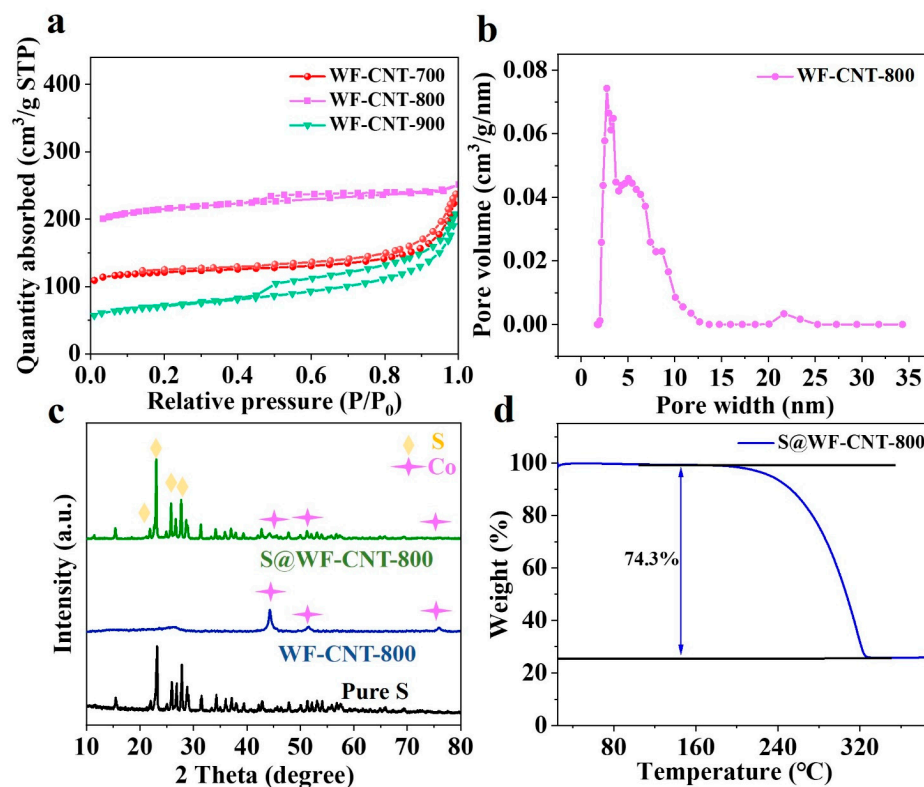
Figure 3. (**a**) Nitrogen adsorption–desorption isotherms of WF-CNT material; (**b**) the corresponding pore-size distribution curves of the WF-CNT-800 composite; (**c**) XRD patterns of pure S, WF-CNT-800, and S@WF-CNT-800 composites; and (**d**) TGA curve of S@WF-CNT-800 composite.
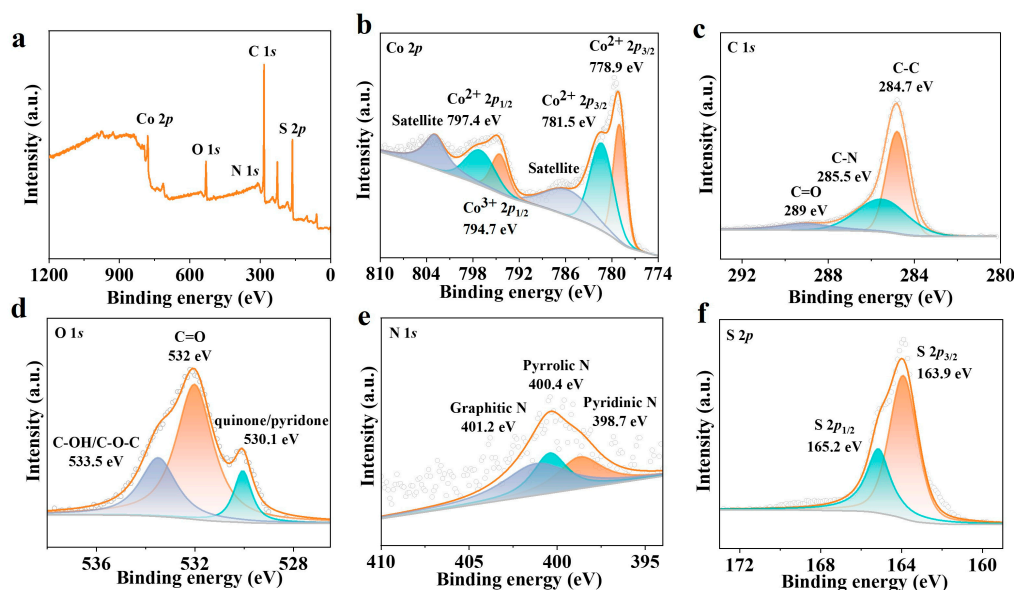
Figure 4. (**a**) Survey spectrum of S@WF-CNT-800 and high-resolution XPS spectra of (**b**) Co 2*p*, (**c**) C 1*s*, (**d**) O 1*s*, (**e**) N 1*s*, and (**f**) S 2*p*.

3.2. Electrochemical Performance of Li–S Batteries

The remarkable electrochemical performance of the S@WF-CNT-800 cathode can be attributed to the unique attributes of its low-tortuosity microchannels and the presence of a free-standing conductive framework. These structural features facilitated rapid ion transfer and, as a result, enhanced the overall electrochemical behavior of the system. The electrochemical reaction processes were meticulously investigated, initially commencing with CV using a voltage window ranging from 1.8 V to 2.8 V at a scan rate of 0.1 mV s^{-1}, as shown in Figure 5a. During the initial scan, two distinct reduction peaks appeared at 2.30 and 2.01 V, corresponding to the reduction of sulfur (S_8) to form long-chain LiPSs (Li_2S_n, where $4 \leq n \leq 8$) and their subsequent reduction to short-chain Li_2S_2 or Li_2S [47,48]. Notably, the first reduction peak at 2.30 V in the first cycle was slightly lower than in the subsequent cycles. This observation reflects a heightened kinetic barrier for the conversion of sulfur to LiPSs during the first cycle. The presence of a broad continuous anodic peak at around 2.45 V signified the oxidation reaction from Li_2S_2/Li_2S to Li_2S_8/S_8. Following the initial scan, no significant alterations in peak positions or currents occurred in subsequent cycles, indicating the effective entrapment of soluble LiPSs by the WF-CNT framework. Figure 5b illustrates the discharge/charge curves, closely mirroring the CV curves. These curves reveal two distinct plateaus characteristic of Li–S batteries, where the elevated plateau corresponds to the reduction of S_8 to LiPSs, while the lower plateau signifies their subsequent reduction to the final products of Li_2S [49]. Additionally, these curves demonstrated minimal polarization even after 100 cycles, emphasizing the stable and efficient electrochemical performance of the system. The cycling performance of S@WF-CNT composites with a sulfur loading of 2 mg$_s$ cm^{-2}, operated at a current density of 0.5 A g^{-1}, is presented in Figure 5c. Notably, the S@WF-CNT-800 sample stood out, delivering the best cycling stability. It exhibited a remarkable initial discharge capacity of 1438.2 mAh g^{-1}, surpassing other samples in the study, including S@WF-600 (927.1 mAh g^{-1}), S@WF-CNT-700 (1004.3 mAh g^{-1}), and S@WF-CNT-900 (762.8 mAh g^{-1}). After 100 cycles, the S@WF-CNT-800 sample retained its superiority, delivering the highest capacity of 588.6 mAh g^{-1} at a high current density of 0.5 A g^{-1}. The success of the S@WF-CNT-800 sample can be attributed to the advantages offered by the low-tortuosity microchannels of the WF, which reduced ion diffusion paths, thus enabling the unhindered movement of the electrolyte within the cathode while accommodating the volumetric changes of sulfur. Additionally, the S@WF-CNT-800 sample boasted a well-formed and dense CNT forest on the channel walls. This CNT forest effectively captured soluble LiPSs and catalyzed their redox kinetics, ultimately resulting in the superior electrochemical performance of the system.

The rate performance of the various samples was meticulously evaluated across a range of current densities, spanning from 0.2 C to 5 C, in order to comprehensively assess their dynamic electrochemical behavior. As illustrated in Figure 5d, the S@WF-CNT-700, S@WF-CNT-800, and S@WF-CNT-900 samples displayed distinctive discharge capacities at 0.2 C, amounting to 1143.5, 1250.1, and 993.7 mAh g^{-1}, respectively. Among these composite materials, the S@WF-CNT-800 sample exhibited the most impressive rate capability, maintaining a reversible capacity of 553.0 and 479.8 mAh g^{-1}, even at elevated current densities of 1 C and 3 C, respectively. Remarkably, when the current density reverted to 0.2 C, the discharge capacity was substantially restored to 954.2 mAh g^{-1}. This phenomenon underscored the outstanding structural stability of the electrodes across varying rates, a crucial factor for the practical implementation of energy storage systems. The EIS curves, as illustrated in Figure 5e, corroborate the aforementioned analysis, with the S@WF-CNT-800 sample exhibiting the lowest charge transfer resistance. This finding further underscores the superior rate performance of the S@WF-CNT-800 composite. The exceptional performance of the S@WF-CNT-800 sample can be attributed to the incorporation of N, O co-doped CNTs within the WF-CNT framework, which played a pivotal role in effectively entrapping LiPSs, resulting in robust chemical and physical interactions with LiPSs. Furthermore, the S@WF-CNT-800 electrodes achieved impressive areal sulfur loadings of 5 mg$_s$ cm^{-2} and 10 mg$_s$ cm^{-2}, further highlighting their practical potential. As demonstrated in Figure 5f,

the cell equipped with the S@WF-CNT-800 cathode maintained a capacity of 348.5 mAh g^{-1} after 100 cycles, even at the high areal sulfur loading of 10 mg$_s$ cm^{-2}. Additionally, the discharge/charge curves and the long-term cycling performance of the S@WF-CNT-800 cathode, with areal sulfur loading of 5 mg$_s$ cm^{-2}, are presented in Figure 5g,h. Notably, these curves reveal manageable polarization voltages even under the sulfur loading condition of 5 mg$_s$ cm^{-2}. Furthermore, a remarkable reversible capacity of 404.5 mAh g^{-1} was achieved after 500 cycles at a current density of 0.5 A g^{-1}, demonstrating the impressive longevity and stability of the S@WF-CNT-800 cathode. Furthermore, Table S1 illustrates the comparative electrochemical performance of CNT-related cathodes for Li-S batteries. Notably, the performance of S@WF-CNT-800 surpassed that of most other CNT-related cathodes. In summary, the comprehensive assessment of rate performance, areal sulfur loading, and extended cycling behavior underscores the exceptional electrochemical potential of the S@WF-CNT-800 composite. These findings highlight its suitability for advanced energy storage applications, particularly in the context of Li–S battery technology, where both performance and stability are paramount.
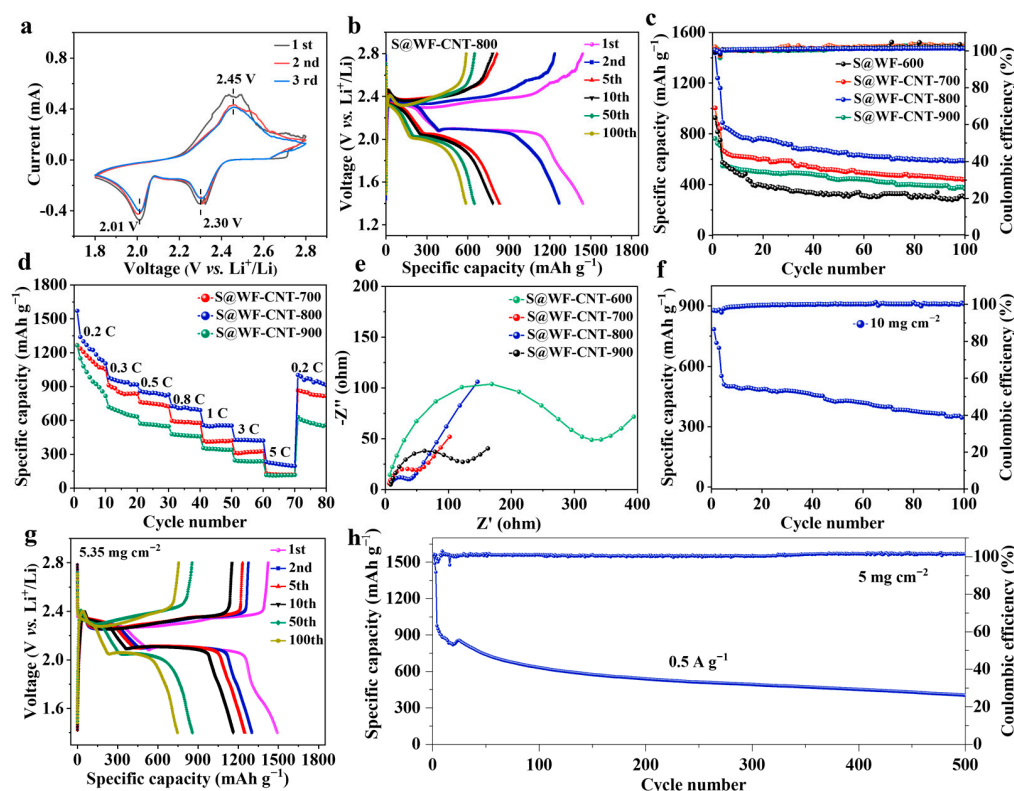
Figure 5. (**a**) CV curves of S@WF-CNT-800; (**b**) charge and discharge curves of S@WF-CNT-800 with sulfur loading of 2 mg$_s$ cm^{-2} at 0.5 A g^{-1}; (**c**) cycle performance; (**d**) rate performance; (**e**) EIS curves of S@WF-CNT at different temperatures; (**f**) cyclability of S@WF-CNT electrodes with sulfur loading of 10 mg$_s$ cm^{-2} at 0.5 A g^{-1}; (**g**) charge and discharge curves of S@WF-CNT-800 with sulfur loading of 5 mg$_s$ cm^{-2} at 0.5 A g^{-1}; and (**h**) cycling performance of S@WF-CNT-800 with sulfur loading of 5 mg$_s$ cm^{-2} at 0.5 A g^{-1}.

4. Conclusions

In conclusion, the innovative design of a low-tortuosity WF-CNT framework, derived from a readily available and cost-effective biomass precursor, has been achieved through a straightforward heat-treatment process. This framework has successfully enabled the development of a high areal sulfur loading cathode, a critical advancement in the realm of energy storage technology. The resulting free-standing sulfur cathode, characterized by its robust mechanical strength, offers a multifaceted array of benefits. It not only serves to

shorten the ion diffusion pathways within the cathode but also significantly enhances the chemical adsorption of LiPSs. As a direct outcome of this innovative approach, the S@WF-CNT-800 sample has emerged as a stand-out candidate, delivering an impressive initial discharge capacity of 1438.2 mAh g^{-1}, even at a high current density of 0.5 A g^{-1}, while maintaining sulfur loading of 2 mg$_s$ cm^{-2}. Furthermore, the sulfur loading capacity has been elevated to 5 mg$_s$ cm^{-2} and 10 mg$_s$ cm^{-2}, underscoring the adaptability and versatility of the electrode design. Importantly, this innovative cathode design shows remarkable cyclic stability, as evidenced by a reversible capacity of 404.5 mAh g^{-1} after an extensive 500 cycles at a current density of 0.5 A g^{-1} with sulfur loading of 5 mg$_s$ cm^{-2}. The profound implications of this electrode architecture design in a cost-effective manner extend beyond the confines of this study. The design offers valuable insights and a promising avenue for the development of high-energy-density batteries, promising cost-effective and sustainable solutions to address the ever-growing demands for advanced energy storage technologies.

Supplementary Materials: The following supporting information can be downloaded at https://www.mdpi.com/article/10.3390/batteries9120594/s1, Figure S1. SEM images of (a–c) WF-600, (d–f) WF-CNT-700, and (g–i) WF-CNT-900. Figure S2. SEM images of the WF-CNT-800 host of (a) vertical section and (b) cross-section. Table S1. Electrochemical performance comparison of CNT-related cathodes for Li-S batteries. References [50–57] are cited in the supplementary materials.

References

1. Zhang, Y.; Wang, N.; Sun, C.; Lu, Z.; Xue, P.; Tang, B.; Bai, Z.; Dou, S. 3D spongy CoS$_2$ nanoparticles/carbon composite as high-performance anode material for lithium/sodium ion batteries. *Chem. Eng. J.* **2018**, *332*, 370–376. [CrossRef]
2. Xue, P.; Wang, N.; Fang, Z.; Lu, Z.; Xu, X.; Wang, L.; Du, Y.; Ren, X.; Bai, Z.; Dou, S. Rayleigh-instability-induced bismuth nanorod@nitrogen-doped carbon nanotubes as a long cycling and high rate anode for sodium-ion batteries. *Nano Lett.* **2019**, *19*, 1998–2004. [CrossRef]
3. Parekh, M.H.; Palanisamy, M.; Pol, V.G. Reserve lithium-ion batteries: Deciphering in situ lithiation of lithium-ion free vanadium pentoxide cathode with graphitic anode. *Carbon* **2023**, *203*, 561–570. [CrossRef]
4. Pang, Q.; Liang, X.; Kwok, C.Y.; Nazar, L.F. Advances in lithium–sulfur batteries based on multifunctional cathodes and electrolytes. *Nat. Energy* **2016**, *1*, 16132. [CrossRef]
5. Lei, J.; Liu, T.; Chen, J.; Zheng, M.; Zhang, Q.; Mao, B.; Dong, Q. Exploring and understanding the roles of Li$_2$S$_n$ and the strategies to beyond present Li-S batteries. *Chem* **2020**, *6*, 2533–2557. [CrossRef]
6. Pope, M.A.; Aksay, I.A. Structural design of cathodes for Li-S batteries. *Adv. Energy Mater.* **2015**, *5*, 1500124. [CrossRef]
7. Bradbury, R.; Dewald, G.F.; Kraft, M.A.; Arlt, T.; Kardjilov, N.; Janek, J.; Manke, I.; Zeier, W.G.; Ohno, S. Visualizing Reaction Fronts and Transport Limitations in Solid-State Li–S Batteries via Operando Neutron Imaging. *Adv. Energy Mater.* **2023**, *13*, 2203426. [CrossRef]
8. Manthiram, A.; Fu, Y.; Chung, S.-H.; Zu, C.; Su, Y.-S. Rechargeable lithium–sulfur batteries. *Chem. Rev.* **2014**, *114*, 11751–11787. [CrossRef]

9. Kim, J.T.; Hao, X.; Wang, C.; Sun, X. Cathode materials for single-phase solid-solid conversion Li-S batteries. *Matter* **2023**, *6*, 316–343. [CrossRef]

10. Demir-Cakan, R.; Morcrette, M.; Nouar, F.; Davoisne, C.; Devic, T.; Gonbeau, D.; Dominko, R.; Serre, C.; Férey, G.; Tarascon, J.-M. Cathode composites for Li–S batteries via the use of oxygenated porous architectures. *J. Am. Chem. Soc.* **2011**, *133*, 16154–16160. [CrossRef]

11. Yin, Y.X.; Xin, S.; Guo, Y.G.; Wan, L.J. Lithium–sulfur batteries: Electrochemistry, materials, and prospects. *Angew. Chem. Int. Ed.* **2013**, *52*, 13186–13200. [CrossRef]

12. Ji, X.; Nazar, L.F. Advances in Li–S batteries. *J. Mater. Chem.* **2010**, *20*, 9821–9826. [CrossRef]

13. Shaibani, M.; Akbari, A.; Sheath, P.; Easton, C.D.; Banerjee, P.C.; Konstas, K.; Fakhfouri, A.; Barghamadi, M.; Musameh, M.M.; Best, A.S. Suppressed polysulfide crossover in Li–S batteries through a high-flux graphene oxide membrane supported on a sulfur cathode. *ACS Nano* **2016**, *10*, 7768–7779. [CrossRef]

14. Kim, H.M.; Sun, H.-H.; Belharouak, I.; Manthiram, A.; Sun, Y.-K. An alternative approach to enhance the performance of high sulfur-loading electrodes for Li–S batteries. *ACS Energy Lett.* **2016**, *1*, 136–141. [CrossRef]

15. Wu, S.; Wang, W.; Shan, J.; Wang, X.; Lu, D.; Zhu, J.; Liu, Z.; Yue, L.; Li, Y. Conductive 1T-VS$_2$−MXene heterostructured bidirectional electrocatalyst enabling compact Li-S batteries with high volumetric and areal capacity. *Energy Storage Mater.* **2022**, *49*, 153–163. [CrossRef]

16. Elazari, R.; Salitra, G.; Garsuch, A.; Panchenko, A.; Aurbach, D. Sulfur-impregnated activated carbon fiber cloth as a binder-free cathode for rechargeable Li-S batteries. *Adv. Mater.* **2011**, *23*, 5641–5644. [CrossRef]

17. Senthil, C.; Jung, H.Y. Molecular polysulfide-scavenging sulfurized–triazine polymer enable high energy density Li-S battery under lean electrolyte. *Energy Storage Mater.* **2023**, *55*, 225–235. [CrossRef]

18. Yan, R.; Mishra, B.; Traxler, M.; Roeser, J.; Chaoui, N.; Kumbhakar, B.; Schmidt, J.; Li, S.; Thomas, A.; Pachfule, P. A Thiazole-linked Covalent Organic Framework for Lithium-Sulphur Batteries. *Angew. Chem. Int. Ed.* **2023**, *62*, e202302276. [CrossRef]

19. Chung, S.H.; Manthiram, A. A polyethylene glycol-supported microporous carbon coating as a polysulfide trap for utilizing pure sulfur cathodes in lithium–sulfur batteries. *Adv. Mater.* **2014**, *26*, 7352–7357. [CrossRef]

20. Zhuang, T.Z.; Huang, J.Q.; Peng, H.J.; He, L.Y.; Cheng, X.B.; Chen, C.M.; Zhang, Q. Rational integration of polypropylene/graphene oxide/nafion as ternary-layered separator to retard the shuttle of polysulfides for lithium–sulfur batteries. *Small* **2016**, *12*, 381–389. [CrossRef]

21. Luo, L.; Chung, S.-H.; Manthiram, A. A trifunctional multi-walled carbon nanotubes/polyethylene glycol (MWCNT/PEG)-coated separator through a layer-by-layer coating strategy for high-energy Li–S batteries. *J. Mater. Chem. A* **2016**, *4*, 16805–16811. [CrossRef]

22. Choi, J.M.; Saroha, R.; Kim, J.S.; Jang, M.R.; Cho, J.S. Porous nanofibers comprising VN nanodots and densified N-doped CNTs as redox-active interlayers for Li–S batteries. *J. Power Sources* **2023**, *559*, 232632. [CrossRef]

23. Cheng, L.; Curtiss, L.A.; Zavadil, K.R.; Gewirth, A.A.; Shao, Y.; Gallagher, K.G. Sparingly solvating electrolytes for high energy density lithium–sulfur batteries. *ACS Energy Lett.* **2016**, *1*, 503–509. [CrossRef]

24. Xing, C.; Chen, H.; Qian, S.; Wu, Z.; Nizami, A.; Li, X.; Zhang, S.; Lai, C. Regulating liquid and solid-state electrolytes for solid-phase conversion in Li–S batteries. *Chem* **2022**, *8*, 1201–1230. [CrossRef]

25. Sun, J.; Zhang, K.; Fu, Y.; Guo, W. Benzoselenol as an organic electrolyte additive in Li-S battery. *Nano Res.* **2023**, *16*, 3814–3822. [CrossRef]

26. Shi, C.; Takeuchi, S.; Alexander, G.V.; Hamann, T.; O'Neill, J.; Dura, J.A.; Wachsman, E.D. High Sulfur Loading and Capacity Retention in Bilayer Garnet Sulfurized-Polyacrylonitrile/Lithium-Metal Batteries with Gel Polymer Electrolytes. *Adv. Energy Mater.* **2023**, *13*, 2301656. [CrossRef]

27. Shi, C.; Alexander, G.V.; O'Neill, J.; Duncan, K.; Godbey, G.; Wachsman, E.D. All-Solid-State Garnet Type Sulfurized Polyacrylonitrile/Lithium-Metal Battery Enabled by an Inorganic Lithium Conductive Salt and a Bilayer Electrolyte Architecture. *ACS Energy Lett.* **2023**, *8*, 1803–1810. [CrossRef]

28. Chi, S.S.; Liu, Y.; Song, W.L.; Fan, L.Z.; Zhang, Q. Prestoring lithium into stable 3D nickel foam host as dendrite-free lithium metal anode. *Adv. Funct. Mater.* **2017**, *27*, 1700348. [CrossRef]

29. Xia, S.; Zhang, X.; Liang, C.; Yu, Y.; Liu, W. Stabilized lithium metal anode by an efficient coating for high-performance Li–S batteries. *Energy Storage Mater.* **2020**, *24*, 329–335. [CrossRef]

30. Yao, Y.X.; Zhang, X.Q.; Li, B.Q.; Yan, C.; Chen, P.Y.; Huang, J.Q.; Zhang, Q. A compact inorganic layer for robust anode protection in lithium-sulfur batteries. *InfoMat* **2020**, *2*, 379–388. [CrossRef]

31. Chung, S.-H.; Chang, C.-H.; Manthiram, A. A core–shell electrode for dynamically and statically stable Li–S battery chemistry. *Energy Environ. Sci.* **2016**, *9*, 3188–3200. [CrossRef]

32. Xiao, J. Understanding the Lithium Sulfur Battery System at Relevant Scales. *Adv. Energy Mater.* **2015**, *5*, 1501102. [CrossRef]

33. Wang, M.; Bai, Z.; Yang, T.; Nie, C.; Xu, X.; Wang, Y.; Yang, J.; Dou, S.; Wang, N. Advances in High Sulfur Loading Cathodes for Practical Lithium-Sulfur Batteries. *Adv. Energy Mater.* **2022**, *12*, 2201585. [CrossRef]

34. Huang, Y.; Lin, L.; Zhang, C.; Liu, L.; Li, Y.; Qiao, Z.; Lin, J.; Wei, Q.; Wang, L.; Xie, Q. Recent advances and strategies toward polysulfides shuttle inhibition for high-performance Li–S batteries. *Adv. Sci.* **2022**, *9*, 2106004. [CrossRef]

35. Chen, L.; Wang, J.; Huang, J.; Tu, T.; Li, L. Cost-trivial material contributes greatly: A review of the application of starch in energy storage systems. *J. Energy Storage* **2023**, *73*, 109060. [CrossRef]

36. Jung, D.S.; Ryou, M.H.; Sung, Y.J.; Park, S.B.; Choi, J.W. Recycling rice husks for high-capacity lithium battery anodes. *Proc. Natl. Acad. Sci. USA* **2013**, *110*, 12229–12234. [CrossRef]
37. Xia, Y.; Xiao, Z.; Dou, X.; Huang, H.; Lu, X.; Yan, R.; Gan, Y.; Zhu, W.; Tu, J.; Zhang, W. Green and facile fabrication of hollow porous MnO/C microspheres from microalgaes for lithium-ion batteries. *ACS Nano* **2013**, *7*, 7083–7092. [CrossRef]
38. Wang, F.; Zhang, L.; Zhang, Q.; Yang, J.; Duan, G.; Xu, W.; Yang, F.; Jiang, S. Electrode thickness design toward bulk energy storage devices with high areal/volumetric energy density. *Appl. Energy* **2021**, *289*, 116734. [CrossRef]
39. Yu, Z.-L.; Yang, N.; Zhou, L.-C.; Ma, Z.-Y.; Zhu, Y.-B.; Lu, Y.-Y.; Qin, B.; Xing, W.-Y.; Ma, T.; Li, S.-C. Bioinspired polymeric woods. *Sci. Adv.* **2018**, *4*, eaat7223. [CrossRef]
40. Chen, C.; Zhang, Y.; Li, Y.; Kuang, Y.; Song, J.; Luo, W.; Wang, Y.; Yao, Y.; Pastel, G.; Xie, J. Highly conductive, lightweight, low-tortuosity carbon frameworks as ultrathick 3D current collectors. *Adv. Energy Mater.* **2017**, *7*, 1700595. [CrossRef]
41. Wang, N.; Zhang, X.; Ju, Z.; Yu, X.; Wang, Y.; Du, Y.; Bai, Z.; Dou, S.; Yu, G. Thickness-independent scalable high-performance Li-S batteries with high areal sulfur loading via electron-enriched carbon framework. *Nat. Commun.* **2021**, *12*, 4519. [CrossRef]
42. He, J.; Lv, W.; Chen, Y.; Xiong, J.; Wen, K.; Xu, C.; Zhang, W.; Li, Y.; Qin, W.; He, W. Direct impregnation of SeS_2 into a MOF-derived 3D nanoporous Co–N–C architecture towards superior rechargeable lithium batteries. *J. Mater. Chem. A* **2018**, *6*, 10466–10473. [CrossRef]
43. Zhu, H.; Zhang, J.; Yanzhang, R.; Du, M.; Wang, Q.; Gao, G.; Wu, J.; Wu, G.; Zhang, M.; Liu, B. When cubic cobalt sulfide meets layered molybdenum disulfide: A core–shell system toward synergetic electrocatalytic water splitting. *Adv. Mater.* **2015**, *27*, 4752–4759. [CrossRef]
44. Lu, Z.; Zhai, Y.; Wang, N.; Zhang, Y.; Xue, P.; Guo, M.; Tang, B.; Huang, D.; Wang, W.; Bai, Z. FeS_2 nanoparticles embedded in N/S co-doped porous carbon fibers as anode for sodium-ion batteries. *Chem. Eng. J.* **2020**, *380*, 122455. [CrossRef]
45. Zhou, X.; Yu, Z.; Yao, Y.; Jiang, Y.; Rui, X.; Liu, J.; Yu, Y. A High-Efficiency Mo_2C Electrocatalyst Promoting the Polysulfide Redox Kinetics for Na-S Batteries. *Adv. Mater.* **2022**, *34*, e2200479. [CrossRef]
46. Song, J.; Xu, T.; Gordin, M.L.; Zhu, P.; Lv, D.; Jiang, Y.B.; Chen, Y.; Duan, Y.; Wang, D. Nitrogen-doped mesoporous carbon promoted chemical adsorption of sulfur and fabrication of high-areal-capacity sulfur cathode with exceptional cycling stability for lithium-sulfur batteries. *Adv. Funct. Mater.* **2014**, *24*, 1243–1250. [CrossRef]
47. Chung, S.H.; Manthiram, A. Current status and future prospects of metal–sulfur batteries. *Adv. Mater.* **2019**, *31*, 1901125. [CrossRef]
48. Huang, J.-Q.; Zhang, Q.; Peng, H.-J.; Liu, X.-Y.; Qian, W.-Z.; Wei, F. Ionic shield for polysulfides towards highly-stable lithium–sulfur batteries. *Energy Environ. Sci.* **2014**, *7*, 347–353. [CrossRef]
49. Xu, R.; Lu, J.; Amine, K. Progress in mechanistic understanding and characterization techniques of Li-S batteries. *Adv. Energy Mater.* **2015**, *5*, 1500408. [CrossRef]
50. Liu, Y.; Li, G.; Chen, Z.; Peng, X. CNT-threaded N-doped porous carbon film as binder-free electrode for high-capacity supercapacitor and Li–S battery. *J. Mater. Chem. A* **2017**, *5*, 9775–9784. [CrossRef]
51. Ma, L.; Zhuang, H.L.; Wei, S.; Hendrickson, K.E.; Kim, M.S.; Cohn, G.; Hennig, R.G.; Archer, L.A. Enhanced Li–S batteries using amine-functionalized carbon nanotubes in the cathode. *ACS Nano* **2016**, *10*, 1050–1059. [CrossRef]
52. Zhou, G.; Wang, D.-W.; Li, F.; Hou, P.-X.; Yin, L.; Liu, C.; Lu, G.Q.M.; Gentle, I.R.; Cheng, H.-M. A flexible nanostructured sulphur–carbon nanotube cathode with high rate performance for Li-S batteries. *Energy Environ. Sci.* **2012**, *5*, 8901–8906. [CrossRef]
53. Lee, J.S.; Jun, J.; Jang, J.; Manthiram, A. Sulfur-immobilized, activated porous carbon nanotube composite based cathodes for lithium–sulfur batteries. *Small* **2017**, *13*, 1602984. [CrossRef]
54. Zhang, Y.; Li, G.; Wang, J.; Luo, D.; Sun, Z.; Zhao, Y.; Yu, A.; Wang, X.; Chen, Z. "Sauna" Activation toward Intrinsic Lattice Deficiency in Carbon Nanotube Microspheres for High-Energy and Long-Lasting Lithium–Sulfur Batteries. *Adv. Energy Mater.* **2021**, *11*, 2100497. [CrossRef]
55. Huang, S.; Zhang, L.; Wang, J.; Zhu, J.; Shen, P.K. In situ carbon nanotube clusters grown from three-dimensional porous graphene networks as efficient sulfur hosts for high-rate ultra-stable Li–S batteries. *Nano Res.* **2018**, *11*, 1731–1743. [CrossRef]
56. Xu, D.W.; Xin, S.; You, Y.; Li, Y.; Cong, H.P.; Yu, S.H. Built-in Carbon Nanotube Network inside a Biomass-Derived Hierarchically Porous Carbon to Enhance the Performance of the Sulfur Cathode in a Li-S Battery. *ChemNanoMat* **2016**, *2*, 712–718. [CrossRef]
57. Shi, Z.; Yang, Y.; Huang, Y.; Yue, H.; Cao, Z.; Dong, H.; Yin, Y.; Yang, S. Organic alkali metal salt derived three-dimensional N-doped porous carbon/carbon nanotubes composites with superior Li–S battery performance. *ACS Sustain. Chem. Eng.* **2019**, *7*, 3995–4003. [CrossRef]